Improved Localization of Cortical Activity by Combining EEG and MEG with MRI Cortical Surface Reconstruction: A Linear Approach

Anders M. Dale and Martin I. Sereno
University of California, San Diego

Abstract

■ We describe a comprehensive linear approach to the problem of imaging brain activity with high temporal as well as spatial resolution based on combining EEG and MEG data with anatomical constraints derived from MRI images. The "inverse problem" of estimating the distribution of dipole strengths over the cortical surface is highly underdetermined, even given closely spaced EEG and MEG recordings. We have obtained much better solutions to this problem by explicitly incorporating both local cortical orientation as well as spatial covariance of sources and sensors into our formulation. An explicit polygonal model of the cortical manifold is first constructed as follows: (1) slice data in three orthogonal planes of section (needle-shaped voxels) are combined with a linear deblurring technique to make a single high-resolution 3-D image (cubic voxels), (2) the image is recursively flood-filled to determine the topology of the gray-white matter border, and (3) the resulting continuous surface is refined by relaxing it against the original 3-D gray-scale image using a deformable template method, which is also used to computationally flatten the cortex for easier viewing. The explicit solution to an error minimization formulation of an optimal inverse linear operator (for a particular cortical manifold, sensor placement, noise and prior source covariance) gives rise to a compact expression that is practically computable for hundreds of sensors and thousands of sources. The inverse solution can then be weighted for a particular (averaged) event using the sensor covariance for that event. Model studies suggest that we may be able to localize multiple cortical sources with spatial resolution as good as PET with this technique, while retaining a much finer grained picture of activity over time. ■

INTRODUCTION

Over the past few decades a variety of techniques for noninvasively measuring brain activity have been developed. Each of these techniques has important and unique advantages, but also significant limitations. For example, the positron-emission tomography (PET) technique using labeled water to detect blood flow has good (~cm), uniform spatial resolution, but relatively poor (~10s of sec) temporal resolution. Several recently developed magnetic resonance imaging (MRI) techniques—measuring blood volume changes with a contrast agent (Belliveau, Kennedy, McKinstry, Buchbinder, Weisskopf, Cohen, Vevea, Brady, & Rosen, 1991) and measuring hemoglobin oxygenation via its effects on nearby water (Ogawa, Tank, Menon, Ellermann, Kim, Merkle, & Ugurbil, 1992)—promise somewhat better spatial and temporal resolution. As with PET, however, the indirect connection between the neural activity and its measured metabolic consequences conceals the fine (subsecond) structure of the underlying neural events.

A widely used technique with better (~msec) temporal resolution is electroencephalography (EEG), which measures the potential difference between various locations on the scalp. A number of interesting correlations between features of the measured waveforms and various aspects of attention, memory, and linguistic tasks have been discovered (see, e.g., Luck & Hillyard, 1990; van Petten & Kutas, 1991; Neville, Nicol, Barss, Forster, & Garrett, 1991). The temporal resolution of this technique is essentially limited only by the time scale of the biological processes producing the potentials. The spatial resolution, however, is limited by several factors. One problem is that activity in a small region of the brain—especially if it is located deep inside the head—can produce potentials that are spread rather widely across the scalp, strongly overlapping potentials produced by other sources.

Closely related to EEG is magnetoencephalography (MEG), which measures minute fluctuations in the magnetic field outside the head using extremely sensitive (SQUID) sensors (see, e.g., Wood, Cohen, Cuffin, & Allison, 1985; Hari & Lounasmaa, 1989; Pantev, Hoke, Lehnertz, Lutkenhoner, Fahrendorf, & Stober, 1990; Wood, George, Lewis, Ranken, & Heller, 1990). The EEG and MEG are fundamentally related through Maxwell's equations to the distribution of dipole moment throughout the brain and head and hence have similar temporal

resolution. However, the MEG has the advantage of being less affected by head inhomogeneities, and somewhat less smeared out spatially by skull impedance than the EEG. On the other hand, a weakness of the MEG is its relative insensitivity to deep or radially oriented sources, making it effectively blind to certain patterns of activity in the brain that would produce an observable EEG.

The so-called *forward problem* of calculating the electric and magnetic fields outside the head, given the current distribution inside the head and the conductive properties of the head and brain, is a well-defined problem of electrostatics (Nunez, 1981). By contrast, the so-called *inverse problem* of finding the distribution of currents inside the head, based on electric and magnetic recordings outside the head, is fundamentally ill-posed—that is, it has no unique solution. For any set of measurements outside the head, there are infinitely many current distributions inside the head that are compatible with those recordings. Although combining both electric and magnetic data about the same event reduces the space of indistinguishable solutions, additional constraints are needed in order to make the problem solution unique in a principled way. Additional constraints come from assumptions about likely current source distributions and statistics, sensor statistics, and information from other activity imaging techniques like PET or functional MRI.

In the following we will present a single framework for combining data from (1) EEG and MEG recordings (and PET or functional MRI, if available), (2) cortical surface reconstructions based on MRI images, (3) prior assumptions about typical spatial distributions of brain activity, and (4) information about covariance of the sensors for a particular (averaged) event. Our primary goal is to retain a linear approach, but constrain it so that the ill-posedness of the inverse problem is greatly reduced. A particularly insidious type of ill-posedness is when sources cancel each other, leading to equivalent solutions that are qualitatively very different. Our studies suggest that the ill-posedness that remains is usually benign; nearby sources may not be resolved, but the qualitative structure of the solution is preserved. By solving directly onto the cortical manifold, it is much easier to assess and view solutions, especially after the cortex has been partially "inflated" (PET or functional MRI data by themselves could also advantageously be viewed this way).

Several components of the current approach to the inverse problem have been considered individually by other authors (Nunez, 1981; Scherg, 1989; Ioannides, Bolton, & Clarke, 1990; Smith, Dallas, Kullmann, & Schlitt, 1990; Wood et al., 1990; Mosher, Lewis, & Leahy, 1992; George, Lewis, Ranken, Kaplan, Aine, & Wood, 1992; Greenblatt, personal communication). By integrating multiple constraints into a unitary framework, however, we have been able to obtain much better behaved solutions than those obtained with any technique used by itself. Model studies suggest that we may be able to localize multiple cortical sources with spatial resolution comparable to PET or functional MRI while retaining a fine-grained picture of activity over time.

A LINEAR APPROACH TO THE INVERSE PROBLEM

In the typical frequency range of neural electric activity of less than a few hundred Hz, the electric and magnetic fields of the brain can be well accounted for by the quasistatic case of Maxwell's equations—that is, magnetic induction and capacitive effects are negligible (Nunez, 1981). As has been noted previously by numerous authors, this results in a simple linear relationship between the electric and magnetic recordings, and the components of dipole moment at any location in the brain. More precisely, if we divide the brain volume into $N/3$ small volume elements and approximate the local dipole moment within each volume element with its decomposition onto three orthogonal components, we get

$$v_i = \sum_j^N e_{ij} s_j \tag{1}$$

or in matrix form

$$\mathbf{v} = \mathbf{E}\mathbf{s} \tag{2}$$

where v_i is the potential at the ith electrode relative to a point at infinity, and s_j is the strength of the jth dipole component. The ith *row* of the **E** matrix specifies the *lead field* of the ith electrode, i.e., how the potential at the ith electrode varies with the strength of each dipole component. The sum in Eq. (1) ranges over all three dipole components of all volume elements. Similarly, the jth *column* of **E** specifies the *gain vector* for the jth dipole component, i.e., how much the measurement at each electrode varies with the strength of the jth component. The coefficients in **E** are in general complicated nonlinear functions of the electrode locations, and the shape and electrical properties of the head (see Appendix A).

For the magnetic recordings we have

$$m_i = \sum_j^N b_{ij} s_j \tag{3}$$

or in matrix form

$$\mathbf{m} = \mathbf{B}\mathbf{s} \tag{4}$$

where m_i is the component of the magnetic field along the orientation of the ith magnetic sensor. The columns of the matrix **B** specify the magnetic gain vector of each dipole component.

Note that Eqs. (2) and (4) can be combined into one equation expressing the linear relationship between each dipole component strength and the composite electric and magnetic recordings:

$$\mathbf{x} = \mathbf{As}, \quad \text{where } \mathbf{x} = \begin{bmatrix} \mathbf{v} \\ \mathbf{m} \end{bmatrix} \quad \text{and } \mathbf{A} = \begin{bmatrix} \mathbf{E} \\ \mathbf{B} \end{bmatrix} \tag{5}$$

More generally, if we assume additive noise at the sensors, we get

$$\mathbf{x} = \mathbf{As} + \mathbf{n} \tag{6}$$

where $\mathbf{n}$ is a zero-mean random vector.[1]

Inverse Solution

The inverse problem can be stated as one of finding the distribution of dipole strength $\mathbf{s}$ given recording data $\mathbf{x}$. Clearly, if the variance of the noise is nonzero, there will exist no well-defined solution to this problem. Also, since the rank of $\mathbf{A}$ is always less than or equal to the number of sensors, there will exist infinitely many indistinguishable solutions whenever the number of unknowns (dipole components) exceeds the number of knowns (sensor locations). However, if a priori information exists about the statistical distribution of dipole moment and sensor noise, the inverse problem can be stated in terms of statistical estimation theory. In the linear case, this corresponds to finding the linear operator that minimizes the expected difference between the estimated and the correct solution. More specifically, the expected error $Err_{\mathbf{W}}$ can be defined as

$$Err_{\mathbf{W}} = \langle \| \mathbf{Wx} - \mathbf{s} \|^2 \rangle \tag{7}$$

where $\mathbf{W}$ is a linear operator that maps a recording vector $\mathbf{x}$ into an estimated solution vector $\hat{\mathbf{s}}$. If we assume that both the noise vector $\mathbf{n}$ and the dipole strength vector $\mathbf{s}$ are normally distributed with zero mean and covariance matrices $\mathbf{C}$ and $\mathbf{R}$, respectively, Eq. (7) becomes

$$Err_{\mathbf{W}} = \langle \| \mathbf{W}(\mathbf{AS} + \mathbf{n}) - \mathbf{s} \|^2 \rangle \tag{8}$$

$$= \langle \| (\mathbf{WA} - \mathbf{I})\mathbf{s} + \mathbf{Wn} \|^2 \rangle \tag{9}$$

$$= \langle \| \mathbf{Ms} + \mathbf{Wn} \|^2 \rangle, \quad \text{where } \mathbf{M} = \mathbf{WA} - \mathbf{I} \tag{10}$$

$$= \langle \| \mathbf{Ms} \|^2 \rangle + \langle \| \mathbf{Wn} \|^2 \rangle \tag{11}$$

$$= Tr(\mathbf{MRM}^{\mathrm{T}}) + Tr(\mathbf{WCW}^{\mathrm{T}}) \tag{12}$$

This expression can be explicitly minimized by taking the gradient, setting it to zero, and solving for $\mathbf{W}$. This yields an optimal linear estimator,

$$\mathbf{W} = \mathbf{RA}^{\mathrm{T}}(\mathbf{ARA}^{\mathrm{T}} + \mathbf{C})^{-1} \tag{13}$$

The expression for the optimal inverse linear operator $\mathbf{W}$ given in (13) can be shown to be equivalent to the so called minimum-norm solution (Tikhonov & Arsenin, 1977; Hamalainen & Ilmoniemi, 1984), provided the covariance matrices $\mathbf{C}$ and $\mathbf{R}$ are proportional to the identity matrix. This corresponds to the assumption that both the noise at each sensor and the strength of each dipole are independent and of equal variance. An advantage of the present formulation is that any empirical observations or reasonable assumptions about the second order statistics of the sensor noise and the dipole strengths can be explicitly incorporated to constrain the solution.

It is also worth pointing out that evaluating $\mathbf{W}$ from Eq. (13) only requires inversion of a matrix square in the number of knowns (sensors), rather than square in the number of unknowns (dipole components). This is important since the time required to invert an N by N matrix is proportional to N^3, and the number of sensors will typically be much smaller than the large number of dipole components (~10,000) that are required to accurately tile the cortical mantle (see below). The only potentially time consuming part of evaluating $\mathbf{W}$ is the matrix multiplication with $\mathbf{R}$, which in the worst case will take time proportional to the square of the number of dipole components. However, if we conservatively make no a priori assumptions about long-range correlations, then the $\mathbf{R}$ matrix will be very sparse, and the memory and time needed for calculating $\mathbf{W}$ will increase more or less linearly with the number of unknowns.

Error Prediction

An important advantage of the linear estimation approach to the inverse problem is that it is possible to quantify the influence of sensor noise and activity of other dipoles on estimated dipole strengths. More precisely, the ith row of the matrix $\mathbf{M} = \mathbf{WA} - \mathbf{I}$ specifies how much a unit of dipole strength at each dipole location would contribute to the estimation error of the ith dipole. Consequently, the expected squared error of the strength of the ith dipole due to activity of other dipoles is given by $\mathbf{M}_i\mathbf{RM}_i^{\mathrm{T}}$, where $\mathbf{M}_i$ is the ith row of $\mathbf{M}$, and $\mathbf{R}$ is the covariance matrix of the sources. Similarly, the ith row of the matrix $\mathbf{W}$ specifies how much a unit of noise at each sensor contributes to the estimation error of the ith dipole strength. The expected squared estimation error for the ith dipole due to noise is given by $\mathbf{W}_i\mathbf{CW}_i^{\mathrm{T}}$, where $\mathbf{W}_i$ is the ith row of $\mathbf{W}$ and $\mathbf{C}$ is the covariance matrix of the noise.

Such expressions for the likely estimation errors can be quite useful for quantifying confidence intervals for hypothesis testing, as well as for designing sensor configurations that optimize the estimation accuracy in some region of interest. Similar measures are difficult to obtain for iterative nonlinear approaches to the inverse problem without explicit, computationally intractable searches for alternate solutions.

CONSTRAINING THE INVERSE SOLUTION

The inclusion of electric and magnetic data in a single formulation constrains the solution to the inverse problem since these two recording techniques often yield complementary information (see Model Studies below). Nevertheless, many equivalent solutions will remain, even in the presence of a single source, and it is neces-

sary to add additional constraints in the form of a priori information about likely solutions. Ideally, we would like to avoid arbitrary a priori constraints—such as having to decide how many source dipoles the solution will contain (cf. Scherg, 1989). In the following, we describe how more biologically plausible constraints can be incorporated into the linear estimation approach outlined above. Our goal is to constrain our solutions while retaining a relatively "automatic" procedure in which the user is spared sensitive, yet arbitrary decisions.

Using Anatomical Constraints

A crucial way to reduce the ambiguity of the inverse problem is to incorporate anatomical constraints explicitly into the solution (see also Wood et al., 1990; George et al., 1992). We can consider in the forward solution only those dipole locations and orientations that are consistent with the anatomical data.

A common assumption is that much of the EEG and MEG observable at a distance is produced by currents flowing in the apical dendrites of cortical pyramidal cells. Because of the columnar organization of the cortex, the resulting local dipole moment would be oriented perpendicularly to the cortical surface. Subdural and intracortical recordings of field potentials at varying distances from an activated cortical locus are consistent with this picture (see, e.g., Mitzdorf, 1987; Dagnelie, Spekreijse, & van Dijk, 1989; Barth & Di, 1990), in general, having revealed substantial vertical, but little local horizontal variation in potential. Thus, if the shape of the cortical sheet is known, the locations and orientations of cortical sources can be constrained by dividing the sheet into patches that are sufficiently small so that a dipole in the center of a patch accounts for any distribution of dipole moment within the patch. The inverse problem then reduces to estimating the scalar distribution of dipole strength over the oriented cortical patches. This should be compared to the unconstrained situation where we would have to solve onto the orthogonal triples of "regional dipoles" distributed throughout the volume of the forebrain (see, e.g., Smith et al., 1990); for a given number of dipoles, the solution is not only less constrained, but much coarser.

It is important to note that the EEG and MEG may be generated by activity in subcortical structures. To localize such activity correctly, the model must include dipole components in these locations as well as in cortical ones. Since subcortical sources are generally located much farther away from the EEG and MEG sensors than are the cortical sources, the discretization of these regions can be coarser. Some of these structures are laminated and contain cells with elongated dendrites perpendicular to the laminae (e.g., the medial superior olive). In structures without clearly elongated cellular morphology, one "regional" dipole triple in the center of each nucleus may be sufficient to account for any distribution of current flow within it.

Using the Assumed Source Covariance

Another useful type of constraint on the inverse problem comes from a priori information about the correlation between the dipole strength at different locations. For instance, it is probably reasonable to assume that activities in two neighboring patches of cortex are not completely independent, but somewhat positively correlated. If the correlation between any two cortical patches is known, the prior source covariance matrix $\mathbf{R}$ is given by

$$\mathbf{R}_{ij} = \sigma_i \sigma_j Corr(i,j) \tag{14}$$

where σ_i^2 is the variance of the strength of the ith dipole, and $Corr(i,j)$ is the correlation between the strengths of the ith and the jth dipoles. The actual correlation of dipole strength as a function of distance on the cortical surface could be estimated by invasive recordings in animals or in human patients.

Note that if the dipoles are assumed a priori to be completely independent ($Corr(i,j) = 0$, if $i \neq j$), and have the same variance ($\sigma_i^2 = \sigma_j^2$), then the method reduces exactly to the minimum-norm approach mentioned above.

Using the Observed Sensor Covariance

Even after incorporating the constraints described above, localized sources still tend to be smeared out by the inverse solution. Denser sensor arrays help for superficial sources, but deep sources are often displaced to the surface and spread over several gyri (see Model Studies below). An additional powerful constraint on the inverse solution that we now turn to comes from considering the entire time course of the electric and magnetic recordings, rather than just a single time point.

A commonly made assumption is that recordings throughout an epoch are caused by activity in a limited number of locations in the brain, each represented by a single dipole with fixed orientation. For the sake of analysis, it is useful to make the following additional assumptions: (1) the activity of each of the, say, k locations is not completely correlated with the activity in any of the other locations, (2) the gain vectors of the active locations are linearly independent, (3) the sensor noise is additive and white with constant variance σ^2, i.e., $\mathbf{C} = \sigma^2\mathbf{I}$. The sensor covariance matrix

$$\mathbf{D} = \langle \mathbf{x}\mathbf{x}^T \rangle = \sigma^2\mathbf{I} + \sum_i \sum_j \sigma_i \sigma_j Corr(i,j)\mathbf{A}_i\mathbf{A}_j^T \tag{15}$$

where the summations range over all active dipoles, has a singular value decomposition given by

$$\mathbf{D} = \mathbf{U}\Lambda\mathbf{U}^{\mathrm{T}} = [\mathbf{U}_1 \cdots \mathbf{U}_N]\begin{bmatrix}\lambda_1 & 0 & 0\\ 0 & \cdots & 0\\ 0 & 0 & \lambda_N\end{bmatrix}[\mathbf{U}_1 \cdots \mathbf{U}_N]^{\mathrm{T}} \quad (16)$$

The first k column vectors $\mathbf{U}_1 \cdots \mathbf{U}_k$ of $\mathbf{U}$ form an orthonormal basis for the so-called *signal subspace* spanned by the k linearly independent gain vectors for the active locations, and $\mathbf{U}_{k+1} \cdots \mathbf{U}_N$ form an orthonormal basis for the so-called *noise subspace,* defined as the orthogonal complement of the signal subspace. Each eigenvalue λ_i specifies the component of sensor covariance in the direction of the corresponding eigenvector.

The noise subspace projection η_i of a gain vector $\mathbf{A}_i$, which can be written

$$\eta_i = \frac{\mathbf{A}_i^{\mathrm{T}}[\mathbf{U}_{k+1} \cdots \mathbf{U}_N][\mathbf{U}_{k+1} \cdots \mathbf{U}_N]^{\mathrm{T}}\mathbf{A}_i}{\mathbf{A}_i^{\mathrm{T}}\mathbf{A}_i} \quad (17)$$

vanishes for true dipole locations. It remains finite for locations whose gain vectors do not lie entirely within the signal subspace. The locations of the true dipoles can thus be estimated, based on the peaks in a plot of $1/\eta_i$ as a function of location, which is essentially the idea behind the MUSIC algorithm (Mosher et al., 1992).

One limitation of this approach is that it requires a clear-cut separation between signal space and noise space. Since the eigenvalues of the sensor covariance matrix typically decrease smoothly, the choice of eigenvalue threshold is somewhat arbitrary. One way to avoid this problem is by using a more graded notion of noise subspace and signal subspace. For instance, by weighting the projection of the gain vectors onto every eigenvector $\mathbf{U}_i$ of $\mathbf{D}$ by the reciprocal of the corresponding eigenvalue λ_i, a measure can be obtained that is large for any gain vector that has a significant component in a direction of low sensor covariance ("noise subspace" component), without requiring an explicit eigenvalue threshold. More precisely, a new measure ξ_i can be defined as

$$\xi_i = \frac{\mathbf{A}_i^{\mathrm{T}}\mathbf{U}\Lambda^{-1}\mathbf{U}^{\mathrm{T}}\mathbf{A}_i}{\mathbf{A}_i^{\mathrm{T}}\mathbf{A}_i} \quad (18)$$

Note that ξ_i converges to η_i as $\lambda_{1\ldots k} \rightarrow \infty$ and $\lambda_{k+1\ldots N} \rightarrow 1$.

This measure can then be incorporated into the linear estimation framework as something similar to an a priori variance estimate[2] for the ith dipole as

$$\mathbf{R}_{ii} = f\left(\frac{1}{\xi_i}\right) \quad (19)$$

where f is a continuous, nondecreasing function. As before, information about correlation between dipole component strengths of neighboring locations can be coded into the estimated source covariance matrix $\mathbf{R}$ by

$$\mathbf{R}_{ij} = \sqrt{R_{ii}R_{jj}}\, Corr(i,j) \quad (20)$$

Note that if the condition number of $\mathbf{D}$ is close to unity (i.e., all eigenvalues equal), then all $\mathbf{R}_{ii}$ are also equal and this method essentially reduces to the minimum-norm-like approach discussed above. However, if the largest and smallest eigenvalues are significantly different, as is usually the case, this method will assign low a priori variance estimates to dipole components with significant "noise-space" projections, essentially eliminating many of the locations in the brain from consideration. In the model studies that follow, we have chosen $f(x) = x$. However, the localization of deep, point-like sources can be further improved by choosing an $f(x)$ that pushes small arguments closer to zero.

Although the sensor covariance matrix $\mathbf{D}^{\mathrm{T}}$ cannot be measured directly, it can be approximated by $\hat{\mathbf{D}} = 1/n\,[\mathbf{x}_1 \cdots \mathbf{x}_n][\mathbf{x}_1 \cdots \mathbf{x}_n]$, where $\mathbf{x}_1 \cdots \mathbf{x}_n$ are the recording vectors at n different times. With extended epochs of activity, it may be preferable to calculate a new set of $\mathbf{R}_{ii}$'s for each of a series of subepochs to help tease apart nearby sources, since different combinations of sources may be active in different subepochs. Note that Eq. (18) applies only to dipoles whose orientation is known. However, it can be extended to handle "regional dipoles" in a manner similar to that developed in Mosher et al. (1992).

One advantage of integrating a cortical anatomical constraint into our formulation is that it can rule out "ghost" sources that would otherwise appear in between two temporally correlated sources with an unconstrained MUSIC approach—the particular morphology of the cortical sheet greatly reduces the probability of there being an appropriately situated ghost source dipole.

Using PET or Functional MRI Information

Although activity imaging techniques like PET and functional MRI may provide little information about the fine-grained temporal sequence of brain activity, they do provide information about average brain activity with relatively high and uniform spatial resolution. It may be reasonable to assume that regions in the brain that show increased activity using metabolic techniques are also ones that are on the average more electrically active over time. Thus, a simple way to incorporate these data into the framework outlined above is to make the prior variance estimate for a location in the brain an increasing function of the PET or functional MRI values at that location. It would clearly be preferable to have a more precise, empirically based model of how the processes that affect PET and functional MRI signals (e.g., cerebral blood flow or hemoglobin oxygenation) are related to the current dipole distribution of the EEG and MEG.

FINDING THE CORTICAL SURFACE

For the approach described above to be practically useful, the shape of the cortical sheet (and the location of

possible subcortical sources) must be known. Since the precise geometry of the cortical manifold varies substantially among different people, it is essential to be able to reconstruct the cortical sheet of each subject using non-invasive imaging techniques, like MRI. This poses two daunting challenges: (1) the MRI data have to have sufficient spatial resolution in all directions to resolve all the sulci and gyri, while also providing sufficient contrast between the relevant tissue types, and (2) a computationally tractable algorithm has to be developed for automatically constructing a wire-frame representation of the cortical sheet based on the MRI data.

Three-Dimensional MRI Reconstruction

With conventional two-dimensional MRI, it is possible to obtain images with excellent contrast between most relevant tissue types, like cortical gray and white matter, cerebrospinal fluid, skull, and scalp with an in-plane resolution of better than 1 mm. However, the resulting 2-D sections are usually relatively thick (e.g., 3–6 mm). Thus, the resolution in the direction perpendicular to the plane of section is much poorer than within the plane—individual volume elements (voxels) are elongated. This causes problems whenever the cortical surface deviates from being nearly perpendicular to the slice plane; single voxels will then average gray and white matter together, generating a smeared image of the cortical mantle.

Using so-called *volume acquisition* techniques, it is theoretically possible to achieve resolutions of 1 mm in all directions. Unfortunately, current volume acquisition protocols are inherently less flexible than the protocols possible with 2-D scans (since each pulse excites the entire volume of the brain, interleaving is not possible, restricting protocols to smaller flip angles and shorter TR values). On the standard MRI scanner available to us for this study, the contrast between cortical gray and white matter possible with an optimal 2-D inversion recovery (IR) protocol was far superior to that possible using volume acquisition. Since the tessellation of the cortex depends on a clear gray/white matter distinction (see below), we had to find a way to overcome the "partial-voluming" problem.

We have developed a method for combining three orthogonal (coronal, sagittal, horizontal) series of conventional, moderately thick sections into a single volumetric data set with the same high (i.e., subslice) resolution in all three directions. The method is based on the simple observation that each pixel in a typical 2-D scan represents a weighted average of the signal emitted from an elongated rectangular prism of tissue (pixel x-size by pixel y-size by slice thickness). By combining data from different directions it is possible to estimate the signal emitted from cubic voxels of smaller size using a linear estimation technique very similar to that described above for current source localization (see Appendix B).

A major advantage of this technique is that any 2-D acquisition protocol can be used, including inversion recovery (IR) protocols for T1 weighting, and spin-echo (SE) protocols with long repetition times for proton-density and T2 weighting. By combining spatially registered 3-D data sets made with different protocols, it is possible to simultaneously classify all major tissue types, which is not possible using any single scan type (cf. Buxton & Greensite, 1991). Thus, we can retain optimal gray/white matter contrast (crucial for cortical surface reconstruction) while still being able to distinguish gray and white matter from skull, skin, and cerebrospinal fluid (necessary for automatic skull removal).

Figure 1A shows a stack of 6 mm thick coronal T1 weighted (inversion–recovery) slices of the brain (see Methods). The resolution within the section plane is obviously much better than in the anterior–posterior direction. The 3-D reconstruction resulting from combining the sagittal and horizontal slice series with the coronal series is shown in Figure 1B. The resolution in the anterior–posterior direction is greatly improved at only a small cost to the in-plane resolution. Note that this image could have been sectioned in any other (non-orthogonal) plane without a loss in resolution. The three-dimensional reconstructions of the proton density and T2 weighted data sets are shown in Figures 1C and 1D, for comparison. Clearly, the contrast between the gray and white matter is most striking in the T1 image.

Surface Reconstruction by "Shrink-Wrapping"

A very realistic-appearing image of the cortex can be generated by displaying stacked sections using interslice interpolation and transparency (see, e.g., Damasio & Frank, 1991). Such an image, however, cannot be directly used to constrain the orientations of source dipoles. For this, we need to construct a wireframe model that explicitly recovers the topology of the cortical sheet (cf. Carman, 1990; Schwartz, 1990). A typical approach to this problem has been to trace the outline of the cortex in series of 2-D sections, and then use some heuristic algorithm (or a practiced hand) to connect the contours in each section into a continuous surface. The main problems with this approach are (1) it requires considerable manual work for each subject, (2) it has trouble with sulci or gyri that are parallel to the plane of section, (3) the topology of the resulting surface may be incorrect, especially when contours in each section have been made continuous for computational reasons (e.g., in sections where the temporal lobe is "detached"), and (4) the resulting surface is difficult or impossible to unfold accurately.

The method we have developed for reconstructing the cortical surface largely overcomes these problems by adopting an automatic deformable template algorithm (see, e.g., Yuille, 1991). The basic idea behind this

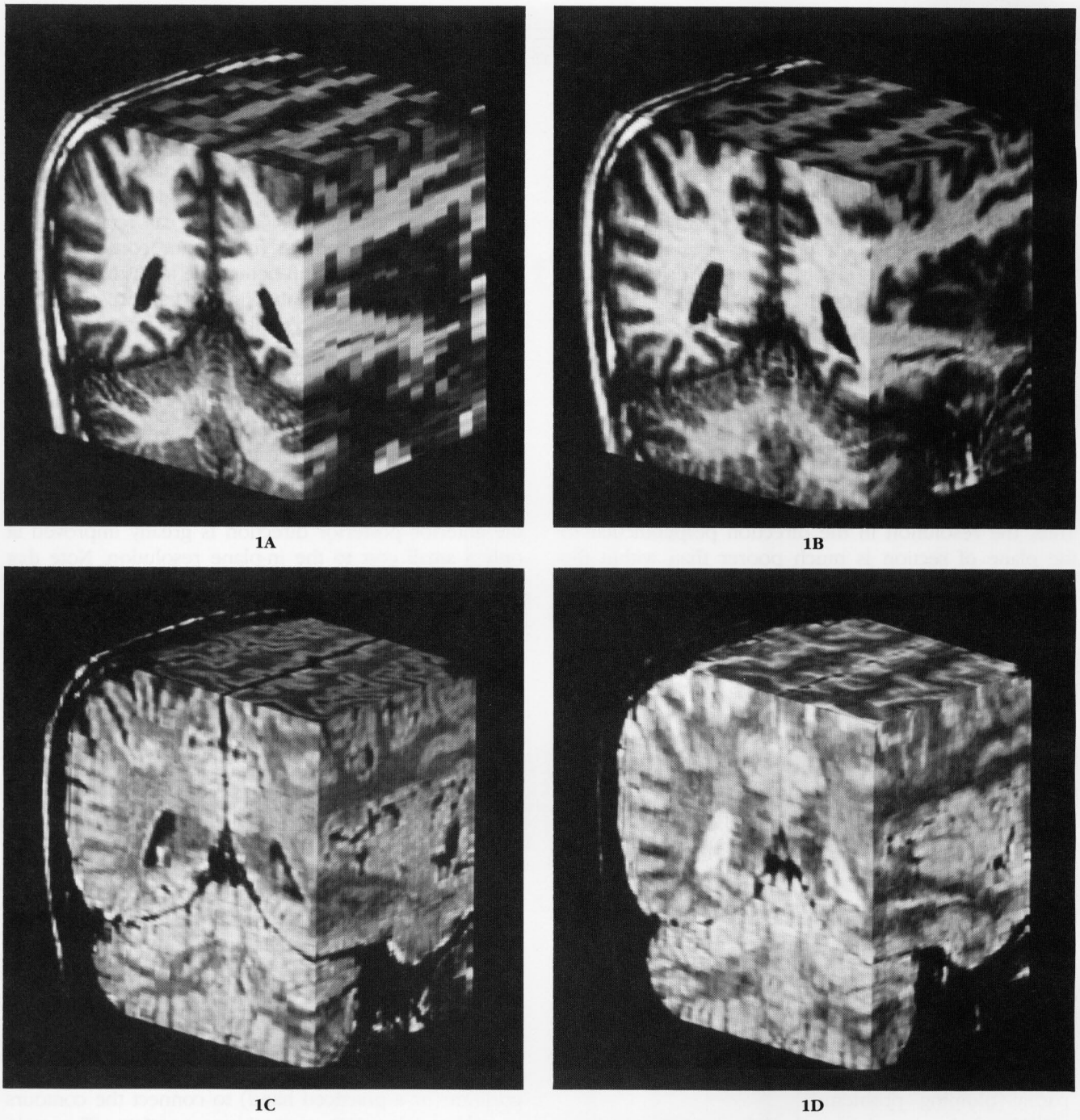

Figure 1. Three-dimensional MRI reconstruction. Coronal sections (6 mm thick) from an inversion recovery protocol are merely stacked in **A**. In **B**, the coronal series has been combined with a horizontal and a sagittal series using a linear deblurring technique to give an image with uniformly high resolution. **C** and **D** illustrate the same deblurring technique applied to proton density and T2-weighted images. The contrast between the gray and white matter is much reduced in comparison to the T1-weighted inversion recovery image.

Figure 2. Surface reconstruction by "shrink-wrapping." An initial closed tessellation of the gray–white matter boundary derived from recursive flood-filling was relaxed onto the 3-D inversion recovery image with the outward force set so that the computed surface rose nearly to the pial surface. The result is shown in **A**. The surface (150,000 polygons) was then released from the MRI data, allowing surface tension to gradually flatten it. Several stages of flattening are shown in **B** (30 iterations), **C** (200 iterations), and **D** (1000 iterations), with green indicating portions of the original folded surface that were convex (~gyri) and red indicating regions that were concave (~sulci). The images in **B–D** were scaled to keep total surface area constant. The major sulcal features are much easier to discern in the partially flattened images.

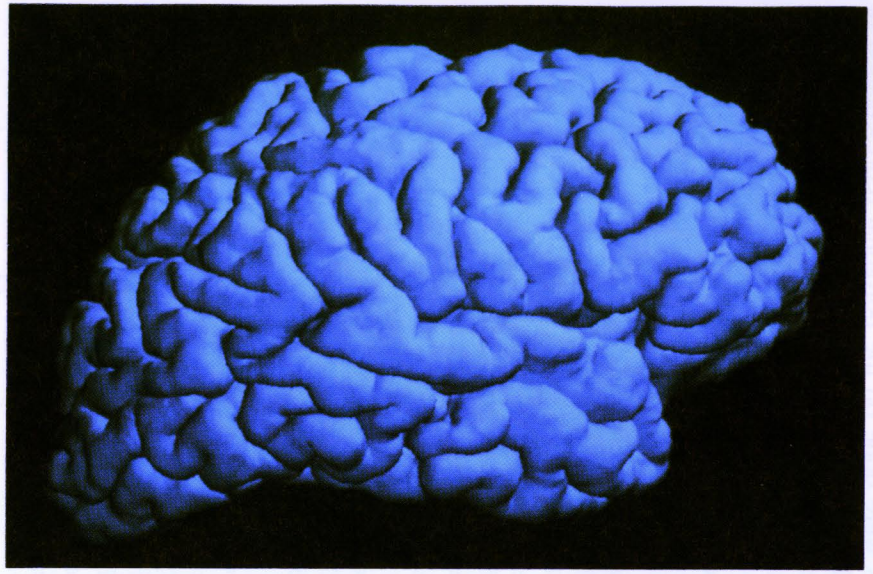

2A

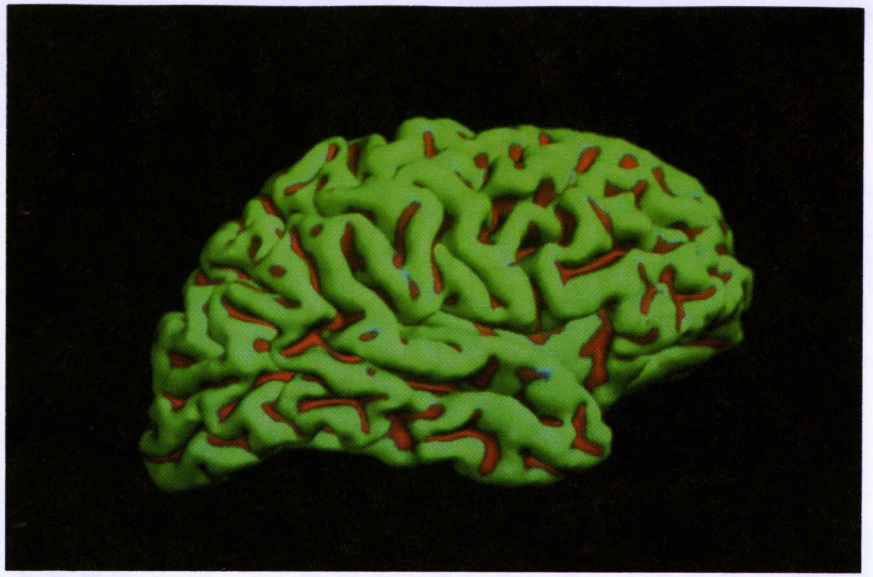

2B

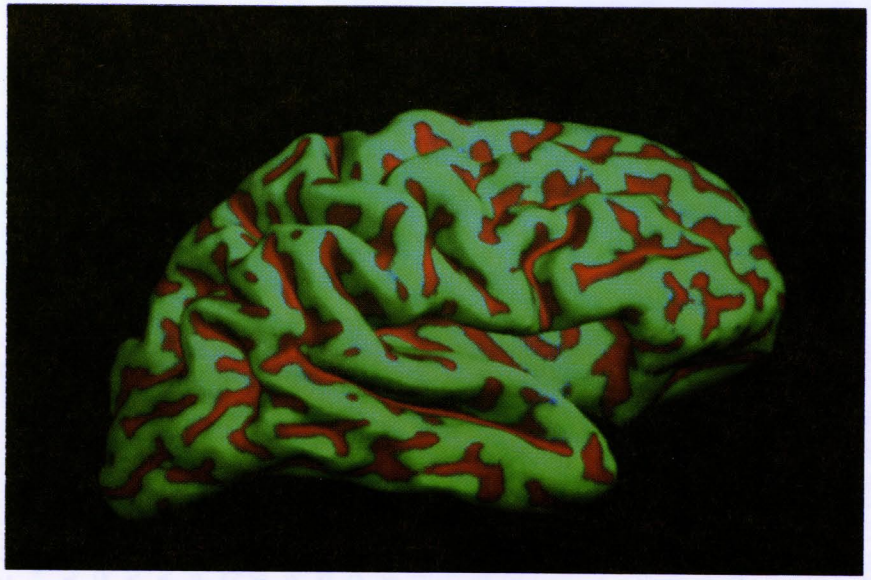

2C

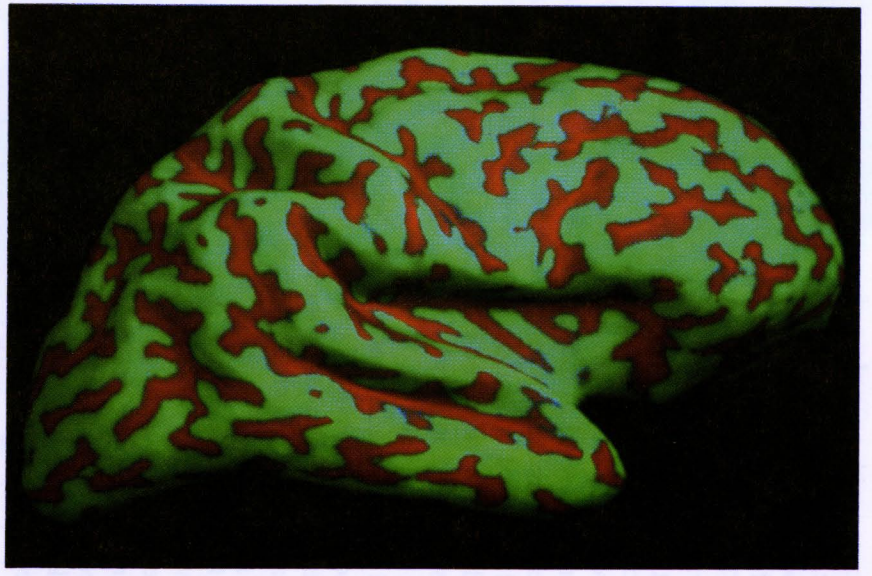

2D

method is to start with a simple surface with the correct topology—e.g, a circle in 2-D, or a spherical shell in 3-D—and then gradually deform the shape of the surface by rubber-sheet transformations to conform to the cortical sheet. The location of each vertex of the surface is updated iteratively according to elastic "forces" between neighboring vertices, and repulsive and attractive forces along the local surface normal depending on the MRI data at the vertex. A nice feature of this technique is that all computations needed in the "shrink-wrapping" process are local. The motion of each vertex can be calculated based on local information about neighboring vertices, and local MRI data. The more global topological constraint is enforced implicitly by the connectivity of the vertices (see Appendix C).

To speed up convergence of the 3-D "shrink-wrap" (and to avoid the computational expense of determining whether the surface has passed through itself at each time step), an initial estimate of the boundary between the cortical gray and white matter was obtained using a three-stage flood-filling algorithm. The white matter of the brain, as classified by MRI data, is initially filled in 3-D from one or more seed locations inside the white matter. Then, a second fill of the volume *outside* the volume filled by the initial fill is performed to eliminate internal holes. Finally, the volume inside the volume filled by the second, external fill is itself filled, to eliminate external islands. The result is a connected volume representation of the white matter. A single, closed tessellation of the white matter surface can then be constructed from the faces of filled voxels bordering unfilled voxels. Figure 2A shows the result of "shrink-wrapping" the initial tessellation of the flood-filled white matter against the MRI data to smooth it. The local repulsive criterion has been set so that the computed surface settles near the surface of the gray matter.

Flattening the Cortex

A straightforward adaptation of the technique described above can be used to computationally flatten the cortical sheet. The surface is relaxed toward minimal surface tension by including only the local elastic forces—i.e., by freeing it from the MRI data. The algorithm will then gradually unfold the cortex while preserving its topology and minimizing local geometric distortions. Figures 2B, 2C, and 2D show snapshots of the cortical surface during the flattening process (after 30, 200, and 1000 iterations; eventually the surface will approach an ellipsoid). In these figures, locations on the initial folded surface with large positive curvature (~sulci) are colored red, while locations with large negative curvature (~gyri) are stained green. Notice how some of the major sulci (e.g., the superior temporal sulcus) that are hard to distinguish from minor ones in the initial folded cortex have become much more conspicuous after a partial flattening. This confirms our experience in physically flattening the cortex of postmortem specimens of the human occipital lobe (Sereno, McDonald, & Allman, 1988; Sereno & Allman, 1991; Sereno, 1991).

A particular advantage of this partially flattened representation is that the cortex retains its global shape, appearing as if it has been gently inflated. This effectively exposes hidden sulcal cortex without the rigors of a complete flattening to a plane, which requires cuts in order to relax the surface, and which is much harder to interpret (see, e.g., Jouandet, Tramo, Herron, Hermann, Loftus, Bazell, & Gazzaniga, 1989). The partially flattened images are quite reminiscent of a macaque brain.

Solutions displayed on such an "inflated" representation are much easier to parse. This representation could easily be adapted to display patterns of activity detected by other techniques like PET or functional MRI; the folded cortical model would simply be colored with the activity data and then inflated.

MODEL STUDIES

In the following we present some results of applying the source localization technique described above to simulated EEG and MEG data. In the 2-D studies the cortical contour was approximated by about 400 vertices and was computed from a coronal MRI image using the "shrink-wrapping" algorithm described above. Similarly, the 3-D studies were done on the polygonal representation of the folded cortical surface, with dipoles at the vertices oriented along the locally estimated surface normal. The original 150,000 vertices of the surface tessellation were evenly subsampled to about 10,000 dipoles, for a spacing between adjacent dipoles of about 4 mm.

The forward transformation matrix **A** was computed based on the locations of the sensors and the location and orientation of each dipole, using the equations for the EEG and MEG given in Appendix A. The results of the 2-D studies are shown on a slightly tilted, shaded 3-D rendering of the "shrink-wrap" solution onto a coronal MRI section, with EEG electrodes and MEG sensors shown as small planar patches in a concentric circular arrangement. The inner circle represents the EEG electrodes and the outer circle represents the MEG sensors. For the 3-D studies, a geodesic arrangement of 61 electric and 61 magnetic sensors was assumed, resulting in an approximately uniform distribution of sensors over the head, for a spacing between sensors of about 40 mm. The sensor coordinates were calculated based on the vertices of a half icosahedron subdivided with a frequency of 3 (see Kenner, 1976). The arrangement was scaled according to the radius of the head, as estimated by half the distance from the nasion to the inion, and rotated so as to align the equator of the arrangement with a line from the nasion to the inion, based on MRI data. Note that this spherical approximation to the head tends to overestimate the distance from sensors on the

lateral parts of the head to the brain, since the head is typically not quite as wide as it is long.

The dipole strengths and recording values are color coded. Positive values are indicated by red, while negative values are indicated by green. The magnitude is coded by the saturation of the color; gray indicates that the value is close to zero, saturated red indicates a large positive value, and saturated green indicates a large negative value.

Single Radial or Tangential Dipole

Figure 3A shows the location of a single superficial, nearly *radial* dipole. Figures 3B, 3C, and 3D show the corresponding linear inverse solution using electric data alone, magnetic data alone, and both kinds of data together. Notice that the solution based on magnetic data alone is much worse than that based on electric data alone.

Figure 4A shows the location of a single superficial, nearly *tangential* dipole. Figures 4B, 4C, and 4D show the corresponding linear inverse solution again for electric data alone, magnetic data alone, and both kinds of data together. The solution based on magnetic data alone is now much better than that based on electric data alone.

Interestingly, even though the MEG by itself is essentially blind to radial sources, it can help rescue radial sources when combined with EEG. This is because it can rule out incorrect alternative interpretations of the EEG data. For example, a radial dipole near a tangential dipole generates a scalp current distribution similar to that produced by a single, laterally displaced radial dipole; adding MEG data picks out the tangential dipole, thus restoring the radial dipole to its rightful location.

Deep Dipole

Figure 5A shows the location of a radial dipole located deep inside the insula. Figure 5B shows the corresponding linear solution using both electrical and magnetic information. This illustrates the well-known problem that minimum-norm-like techniques tend to interpret deep, focal activity as more spread-out, superficial activity.

Figure 5D shows the dramatic improvement in the solution made possible by taking temporal information into account. In this simple case with only a single dipole active, the sensor covariance matrix will be equal to the outer product of the gain vector of the active dipole location with itself plus some multiple of the identity matrix [see Eq. (15)]. We have assumed white noise and a signal-to-noise ratio of 3:1. The variance estimates $\mathbf{R}_{ii}$ for each dipole are shown in Figure 5C.

3-D Studies

The locations of eight assumed sources are illustrated on the unfolded cortex in Figure 6A. The estimated solution shown in Figure 6C (the sensors are omitted) demonstrates that these well-separated sources can all be distinguished. The sensor covariance matrix was computed assuming correlation between each of the sources of 0.5, additive white noise, and a signal-to-noise ratio of 10:1. Figure 6B shows the corresponding calculated variance estimate $\mathbf{R}_{ii}$ for each dipole. Nearby correlated sources will merge, however, if they are close enough to each other. In Figures 7A–C, the similarly signed (green) source pair at the left is beginning to merge. Nearby sources with different signs can sometimes be distinguished at closer distances (red–green pair at right), but will eventually cancel each other if they are close enough (upper red–green pair).

It should also be noted that using sensor covariance information does not always rescue deep sources. If the magnitude of the signal produced by a deep source is too weak compared to the noise, or if there are active superficial sources that could produce a signal close to that of the deep source, some of the activity of the deep source will be attributed to the superficial sources. This uncertainty in the estimate of the strength of a deep source can be detected by analyzing the predicted estimation error as described previously.

CONCLUSION

All known techniques for imaging brain activity have limitations in temporal and spatial resolution. Some of these limitations can be overcome by combining data obtained using different techniques in a way that takes advantage of the strengths of each technique to obtain a single optimal solution. Note that this is very different from finding solutions using each technique independently and then comparing the results. If the solutions are different in that case, it is not clear which part of which solution to trust.

There are a number of advantages of the linear approach over traditional approaches to the problem of source localization and imaging.

1. It provides a principled framework for combining EEG and MEG recording data with information about cortical geometry from MRI.
2. Since it makes no assumptions about the number of equivalent dipole sources, this technique is well suited to situations with many correlated sources of cortical activity.
3. By incorporating an improved soft constraint based on the observed covariance of sensors over time for a particular event, localization of deep sources is greatly improved, without disallowing spread-out solutions.
4. Other sources of data like PET or functional MRI can be easily incorporated.
5. The recovery of the topology of the cortical manifold makes it possible to conveniently view the solutions (as well as data from other activity imaging techniques)

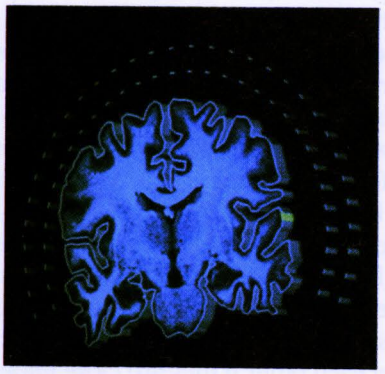

3A

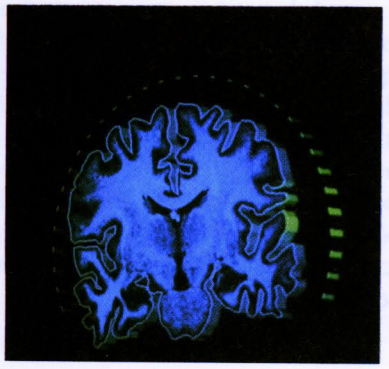

3B

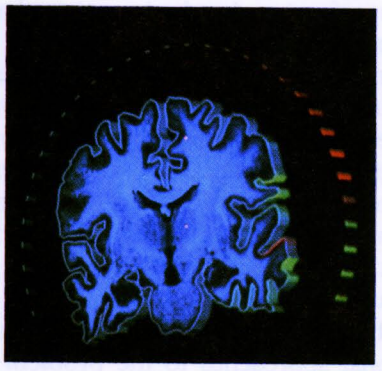

3C

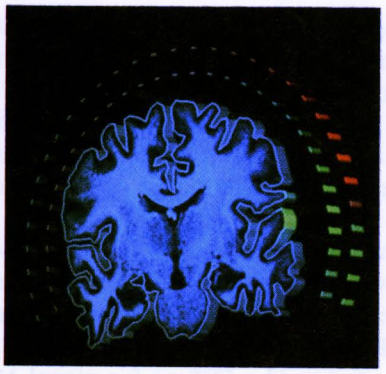

3D

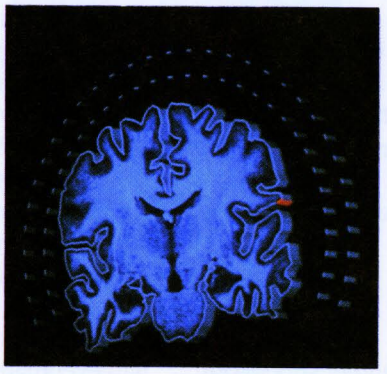

4A

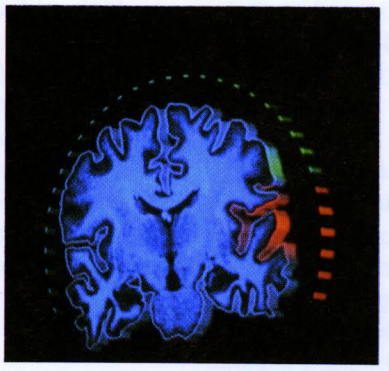

4B

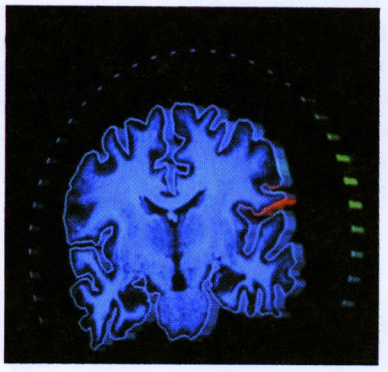

4C

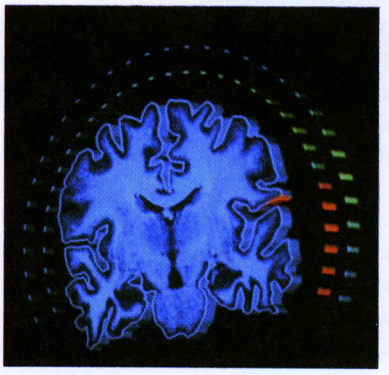

4D

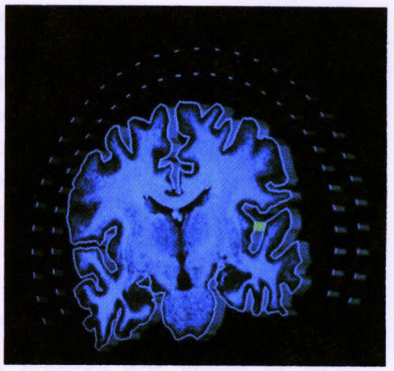

5A

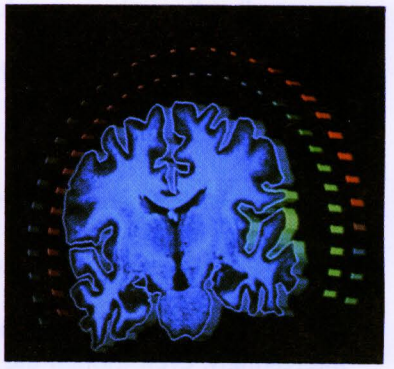

5B

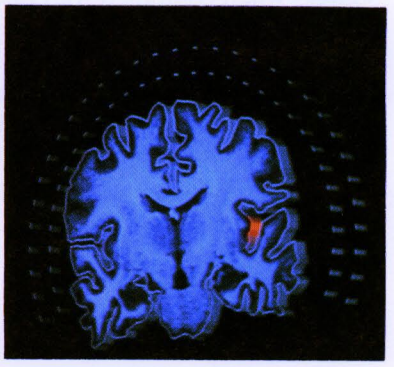

5C

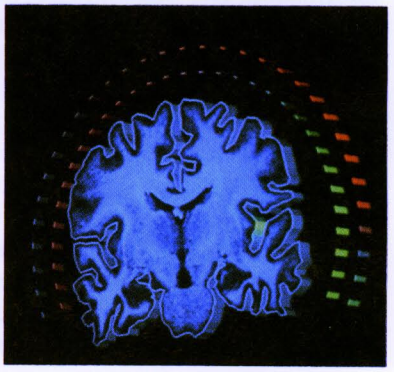

5D

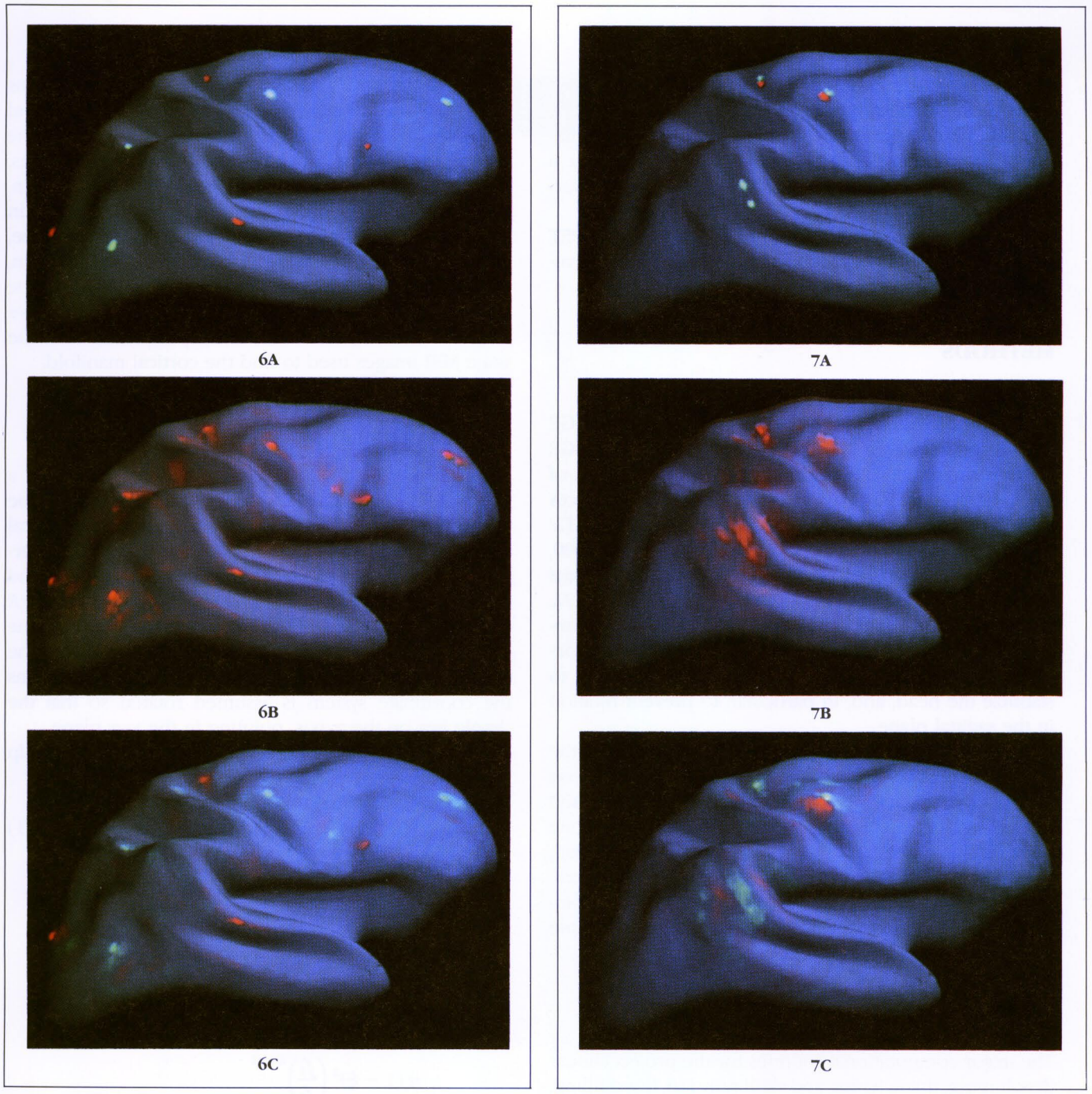

Figure 3. A single superficial, nearly *radial* dipole source is shown in **A**. The forward solutions are shown on the sensors, and the linear inverse solution on the cortical ribbon for electric data alone (**B**), magnetic data alone (**C**), and both kinds of data (**D**). The dipole strengths and recording values are color coded and the inner and outer circles represent the EEG and MEG sensors. Positive values are indicated by red, while negative values are indicated by green. The solution based on magnetic data alone is much worse than that based on electric data alone.

Figure 4. A single superficial, nearly *tangential* dipole source is shown in **A**. The linear inverse solutions for electric data alone (**B**), magnetic data alone (**C**), and both kinds of data (**D**) now show that the solution based on magnetic data alone is much better than that based on electric data alone.

Figure 5. A deep radial source in the insula (**A**) illustrates a well-known problem with minimum-norm-like solutions. Even with both electric and magnetic information, deep focal activity is interpreted as weaker superficial spread-out activity (**B**). Dramatic improvement in the solution results when temporal information is taken into account (**D**). We have assumed white noise and a signal-to-noise ratio of 3:1. The corresponding calculated variance estimates $\mathbf{R}_{ii}$ for each dipole are shown in **C**.

Figure 6. 3-D model studies. The locations of eight sources are displayed on the flattened cortex in **A** (all calculations were performed using the folded cortex). The solution using temporal information is shown in **C** (61 EEG and MEG sensors placed in a geodesic arrangement are omitted; the sensor covariance matrix was computed assuming between-source correlation of 0.5 and additive white noise, with a signal-to-noise ratio of 10; the 150,000 polygon surface was subsampled to about 10,000 dipoles for these solutions). The corresponding calculated variance estimates $\mathbf{R}_{ii}$ for each dipole are shown in **B**.

Figure 7. Nearby sources. Correlated sources can merge if they are close together (between-source correlation of 0.5). The lower left pair of similarly signed sources in **A** are beginning to merge in the variance estimates in **B** and in the solution in **C**; even nearer pairs can be distinguished if they are of opposite sign (lower red–green pair at right), but eventually cancel each other if close enough (upper red–green pair).

after gently "inflating" the brain, as well as allowing more effective intersubject comparisons.

6. The expected error of the solution can be computed for different source configurations, providing a principled way to quantify statistical significance of various hypotheses.

7. The spatial resolution is comparable to that of PET or functional MRI without sacrificing fine-grained temporal resolution.

METHODS

MRI Images

The brain of the second author was scanned on a GE SIGNA system with a 1.5T magnet and the ADVANTAGE software upgrade. The scanning sequence consisted of three orthogonal T1/inversion recovery slice sequences (TR=2000, TI=708, TE=12) and three orthogonal T2/proton density spin-echo slice sequences (TR=2000, TE=11, 70) for a total scan time of 82 min. All scans used a 25-cm field-of-view, a matrix size of 256 × 192, and contiguous 6-mm slices. Since the linear "devoluming" of the images was quite sensitive to movement between successive images, a special effort was made to stabilize the head, and, in particular, to prevent rotation in the sagittal plane.

By evaluating the expression for absolute value of the inversion recovery signal strength (with Mathematica on the NeXT computer) for different repetition (TR) and inversion (TI) times using T1 values for gray and white matter (Mitchell, Conturo, Gruber, & Jones, 1984; Hyman, Kurland, Levy, & Shoop, 1989; Buxton, personal communication), it was possible to search for the TI/TR combination giving the best contrast between these two tissue types.

Software

The major computational routines for the project (linear devoluming, tissue typing and skull removal, flood-filling, surface tessellation, geodesic sensor placement, cortical shrink-wrapping and inflation, forward solution, inverse solution, sensor covariance weighting) were written in C. Display software for the 2-D slice and 3-D cortical surface images was also written in C using Silicon Graphics GL routines, which take advantage of fast hardware implementation of 3-D transformations, polygon filling, and lighting calculations on Silicon Graphics machines.

APPENDIX A: FORWARD CALCULATIONS

In the following we will present the actual equations used in the model studies for calculating the forward solutions for the EEG and MEG. The idealized assumptions made here about head geometry and electrical parameters are not essential for the general linear approach to the inverse problem, since these assumptions affect only the values in the coefficient matrices, **E** and **B**. These are simply treated as arbitrary arguments in the inverse calculations. More realistic forward calculations, based on the exact shape of the scalp, skull, and brain, can be done using finite element methods (FEM), in order to generate more realistic **E** and **B** matrices (see, e.g., Meijs, Bosch, Peters, & Lopes da Silva, 1987; Yan, Nunez, & Hart, 1991). Quantitative estimates of the shape and thickness of the real scalp, skull, and conductive bone sutures are, of course, directly available from the same MRI images used to find the cortical manifold.

EEG Calculations

To calculate the EEG, we assume a single dipole in a three-shell inhomogeneous spherical conductor. The shell model consists of a homogenous sphere of neural tissue with radius r_1, surrounded by a concentric spherical shell of outside radius r_2, representing the skull, and another concentric spherical shell of outside radius R representing the scalp. The scalp and the neural tissue are assumed to have the same conductivity σ, and the skull to have conductivity σ_s. To simplify the calculations the coordinate system is assumed rotated so that the dipole lies on the z-axis, pointing in the x–z plane.

The potential recorded at location (α,β) on the scalp can be expressed as

$$v(\alpha,\beta) = \frac{1}{4\pi\sigma}\sum_{n=1}^{\infty}\frac{2n+1}{n}b\left(\frac{\xi\,(2n+1)^2}{d_n\,(n+1)}\right) \qquad \text{(A.1)}$$

$$(ns_rP_n\cos\alpha + s_tP_n^1\cos\alpha\cos\beta)$$

$$d_n = [(n+1)\,\xi + n]\left(\frac{n\xi}{n+1}+1\right) +$$

$$(1-\xi)\,[(n+1)\,\xi + n]\,(f_1^{2n+1} - f_2^{2n+1})$$

$$-\,n\,(1-\xi)^2\left(\frac{f_1}{f_2}\right)^{2n+1}$$

where $\xi = \sigma_s / \sigma$, $f_1 = r_1 / R$ and $f_2 = r_2 / R$. s_t and s_r are the tangential and radial components of the dipole moment, or strength s. P_n and P_n^1 are the Legendre and the associated Legendre polynomials, respectively (Ary, Klein, & Fender, 1981).

MEG Calculations

Making assumptions similar to those made for the EEG calculations we get the following expression for the radial component of the magnetic field h observed at location (r,α,β) outside the head

$$h(r,\alpha\beta) = \frac{b\sin\alpha\sin\beta\; s_t}{4\pi r^2\gamma^{3/2}} \qquad \text{(A.2)}$$

where

$$\gamma = 1 - \frac{2b \cos \alpha}{r} + \left(\frac{b}{r}\right)^2$$

Somewhat more complicated expressions can be found for the nonradial components of the magnetic field (Cuffin & Cohen, 1977). Note that the magnetic field is independent of the radial component s_r of the dipole.

APPENDIX B: ORTHOGONAL MRI SLICE COMBINATION ("DEVOLUMING")

The intersection between any three orthogonal MRI sections forms a cube, with sides equal to the section thickness (typically several times the in-plane pixel width). Let $\mathbf{v}$ denote the vector of N^3 unknown cubic volume elements (voxels) inside this cube, and let $\mathbf{c}$, $\mathbf{h}$, and $\mathbf{s}$ denote vectors of N^2 known picture elements (pixels) of the coronal, horizontal, and sagittal sides of the cube, respectively. Then, if each pixel in a section reflects the linearly weighted sum of MRI signal from the tissue throughout the thickness of the section, the following "forward" equations hold:

$$\mathbf{c} = \mathbf{C}\mathbf{v}, \quad \mathbf{h} = \mathbf{H}\mathbf{v}, \quad \mathbf{s} = \mathbf{S}\mathbf{v} \tag{B.1}$$

where $\mathbf{C}$, $\mathbf{H}$, and $\mathbf{S}$ are the easily derived linear operators that map N^3 voxel values into N^2 pixel values in the coronal, horizontal, and sagittal planes, respectively. A least-squared-error estimate of $\mathbf{v}$ is then given by

$$\mathbf{v}^* = (\mathbf{C}^T\mathbf{C} + \mathbf{H}^T\mathbf{H} + \mathbf{S}^T\mathbf{S} + \mathbf{R})^{-1} (\mathbf{C}^T\mathbf{c} + \mathbf{H}^T\mathbf{h} + \mathbf{S}^T\mathbf{s}) \tag{B.2}$$

where $\mathbf{R}$ is a regularization matrix, which is typically set equal to a small multiple of the identity matrix.

APPENDIX C: CORTICAL SURFACE REFINEMENT ("SHRINK-WRAPPING")

In the "shrink-wrapping" procedure, the position of each vertex is updated iteratively using a data term and smoothness term according to the following equations:

$$p_i^{(t+1)} = p_i^{(t)} + \alpha F(p_i^{(t)}) n_i^{(t)} + \beta \frac{1}{N_i} \sum_{j \in \aleph_i} v_{ij}^{(t)} \tag{C.1}$$

where

$$n_i = \frac{1}{N_i}[(u_{i,\aleph_i^1} \times u_{i,\aleph_i^2}) + (u_{i,\aleph_i^2} \times u_{i,\aleph_i^3}) + \cdots + (u_{i,\aleph_i^{N_i}} \times u_{i,\aleph_i^1})] \tag{C.2}$$

$$u_{ij} = \frac{v_{ij}}{|v_{ij}|} \tag{C.3}$$

$$v_{ij} = p_j - p_i \tag{C.4}$$

where $p_i^{(t)}$ is the position of the ith vertex at iteration t, $\aleph_i$ is the ordered set of N_i vertices neighboring the ith vertex, $\aleph_i^j$ is the jth element of this set. By convention, the elements of the set $\aleph_i$ are ordered so that the cross products $u_{i,\aleph_i^j} \times u_{i,\aleph_i^{j+1}}$ point toward the outside of the surface. The function $F(p_i)$ determines the repulsive or attractive force acting on the ith vertex in a direction perpendicular to the surface. It typically depends only on the MRI values at the point p_i, taking on a negative (attractive) value for CSF, and a positive (repulsive) value for white matter. In the present study we used $F(p) = \tanh[\gamma(IR(p) - IR_{\text{Gray}})]$, where $IR(p)$ is the inversion recovery image value at location p, IR_{Gray} is the typical inversion recovery image value for cortical gray matter, and γ is a suitably chosen constant.

By varying the parameters α and β it is possible to control the influence of the data term $\alpha F(p_i^{(t)}) n_i^{(t)}$ and the smoothness term

$$\beta \frac{1}{N_i} \sum_{j \in \aleph_i} v_{ij}^{(t)}$$

on the solution. Iterative "flattening" of the surface is achieved by setting α equal to zero, which releases the surface from the data.

Acknowledgments

We would like to thank David Amaral for help and support in obtaining the MRI images and Marta Kutas, Chris Wood, Steven Hillyard, Richard Greenblatt, Rick Buxton, John George, Greg Simpson, Bill Loftus, John Allman, George Carman, Brandt Kehoe, Kechen Zhang, Eric Courchesne, Terri Jernigan, Carsten Lutken, and an anonymous reviewer for help and discussions. Supported by UCSD McDonnell-Pew Cognitive Neuroscience Center grants for research and graduate support.

Notes

1. This does not address the problem of nonadditive "noise" arising from errors in the forward solution (coefficients of the **A** matrix). This noise can be reduced by using a more realistic forward solution (see Appendix A).
2. Leaving out the normalizing denominator in Eq. (18) results in $1/\xi_i$ having the same units as σ_i^2. However, this has the undesirable effect of assigning very large a priori variance estimates for dipole locations with gain vectors of small magnitude (e.g., deep sources).

Reprint requests should be sent to James C. Prechtl, Department of Neurosciences 0201, University of California, San Diego, La Jolla, CA 92093-0201.

REFERENCES

Ary, J. P., Klein, S. A., & Fender, D. H. (1981). Locations of sources of evoked scalp potential: Corrections for skull and scalp thicknesses. *IEEE Transactions on Biomedical Engineering, BME-28,* 447–452.

Barth, D. S., & Di, S. (1990). Three-dimensional analysis of auditory-evoked potentials in rat neocortex. *Journal of Neurophysiology, 64,* 1527–1536.

Belliveau, J. W., Kennedy, D. N., McKinstry, R. C., Buchbinder,

B. R., Weisskopf, R. M., Cohen, M. S., Vevea, J. M., Brady, T. J., & Rosen, B. R. (1991). Functional mapping of the human visual cortex by magnetic resonance imaging. *Science, 254,* 716–719.

Buxton, R. B., & Greensite, F. (1991). Target-point combination of MR images. *Magnetic Resonance in Medicine, 18,* 102–115.

Carman, G. J. (1990). Mappings of the Cerebral Cortex. Ph.D. diss., California Institute of Technology.

Cuffin, B. N., & Cohen, D. (1977). Magnetic fields of a dipole in special volume conductor shapes. *IEEE Transactions in Biomedical Engineering, BME-24,* 372–381.

Dagnelie, G., Spekreijse, H., & van Dijk, B. (1989). Topography and homogeneity of monkey V1 studied through subdurally recorded pattern-evoked potentials. *Visual Neuroscience, 3,* 509–525.

Damasio, H., & Frank, R. (1991). Three-dimensional mapping of brain lesions in the primate brain. *Society for Neuroscience, Abstracts, 17,* 135.

George, J. S., Lewis, P. S., Ranken, D. M., Kaplan, L., Aine, C. J., & Wood, C. C. (1992). Integrated computational models of human brain structure and function. In *Proceedings of the SUN Special Interest Group in Medical Applications,* SIGMA (in press).

Hamalainen, M. S., & Ilmoniemi, R. J. (1984). *Interpreting measured magnetic fields of the brain: Estimates of current distribution.* Helsinki University of Technology, Department of Technical Physics Report TKK-F-A559.

Hari, R., & Lounasmaa, O. V. (1989). Recording and interpretation of cerebral magnetic fields. *Science, 244,* 432–436.

Hyman, T. J., Kurland, R. J., Levy, G. C., & Shoop, J. D. (1989). Characterization of normal brain tissue using seven calculated MRI parameters and a statistical analysis system. *Magnetic Resonance in Medicine, 11,* 22–34.

Ioannides, A. A., Bolton, J. P. R., & Clarke, C. J. S. (1990). Continuous probabilistic solutions to the biomagnetic inverse problem. *Inverse Problems, 6,* 523–542.

Jouandet, M. L., Tramo, M. K., Herron, D. M., Hermann, A., Loftus, W. C., Bazell, J., & Gazzaniga, M. S. (1989). Brainprints: computer-generated two-dimensional maps of the human cerebral cortex in vivo. *Journal of Cognitive Neuroscience, 1,* 88–117.

Kenner, H. (1976). *Geodesic math and how to use it.* Berkeley: University of California Press.

Luck, S. J., & Hillyard, S. A. (1990). Electrophysiological evidence for parallel and serial processing during visual search. *Perception and Psychophysics, 48,* 603–617.

Meijs, J. W. H., Bosch, F. G. C., Peters, M. J., & Lopes da Silva, F. H. (1987). On the magnetic field distribution generated by a dipolar current source situated in a realistically shaped compartment model of the head. *Electroencephalography and Clinical Neurophysiology, 66,* 286–298.

Mitchell, M. R., Conturo, T. E., Gruber, T. J., & Jones, J. P. (1984). Two computer models for selection of optimal magnetic resonance imaging (MRI) pulse sequence timing. *Investigative Radiology, 19,* 350–360.

Mitzdorf, U. (1987). Properties of the evoked potential generators: Current source-density analysis of visually evoked potentials in the cat cortex. *International Journal of Neuroscience, 33,* 33–59.

Mosher, J. C., Lewis, P. S., & Leahy, R. M. (1992). Multiple dipole modeling and localization of spatio-temporal MEG data. *IEEE Transactions on Biomedical Engineering, 39,* 541–557.

Neville, H., Nicol, J. L., Barss, A., Forster, K. I., & Garrett, M. F. (1991). Syntactically based sentence processing classes—evidence from event-related brain potentials. *Journal of Cognitive Neuroscience, 3,* 151–165.

Nunez, P. (1981). *Electric fields of the brain: The neurophysics of EEG.* New York: Oxford University Press.

Ogawa, S., Tank, D. W., Menon, R., Ellermann, J. M., Kim, S. G., Merkle, H., & Ugurbil, K. (1992). Intrinsic signal changes accompanying sensory stimulation: functional brain mapping with magnetic resonance imaging. *Proceedings of the National Academy of Sciences, U.S.A. 89,* 5951–5955.

Pantev, C., Hoke, M., Lehnertz, K., Lutkenhoner, B., Fahrendorf, G., & Stober, U. (1990). Identification of sources of brain neuronal activity with high spatiotemporal resolution through combination of neuromagnetic source localization (NMSL) and magnetic resonance imaging (MRI). *Electroencephalography and Clinical Neurophysiology, 75,* 173–184.

van Petten, C., & Kutas, M. (1991). Influences of semantic and syntactic context on open- and closed-class words. *Memory and Cognition, 19,* 95–112.

Scherg, M. (1989). Fundamentals of dipole source potential analysis. In F. Grandori, G. L. Romani, & M. Hoke (Eds.), *Auditory evoked potentials and fields: Advances in audiology 6.* Basel: Karger.

Schwartz, E. L. (1990). Computer-aided neuroanatomy of macaque visual cortex. In E. L. Schwartz (Ed.), *Computational neuroscience* (pp. 295–315). Cambridge: MIT Press.

Sereno, M. I. (1991). Language and the primate brain. *Proceedings, Thirteenth Annual Conference of the Cognitive Science Society* (pp. 79–84). Hillsdale, NJ: Lawrence Erlbaum Associates.

Sereno, M. I., & Allman, J. M. (1991). Cortical visual areas in mammals. In A. G. Leventhal (Ed.), *The neural basis of visual function* (pp. 160–172). London: Macmillan.

Sereno, M. I., McDonald, C. T., & Allman, J. M. (1988). Myeloarchitecture of flat-mounted human occipital lobe: Possible location of visual area of MT. *Society for Neuroscience, Abstracts, 14,* 1123.

Smith, W. E., Dallas, W. J., Kullmann, W. H., & Schlitt, H. A. (1990). Linear estimation theory applied to the reconstruction of a 3-D vector current distribution. *Applied Optics, 29,* 658–667.

Tichonov, A. N., & Arsenin, V. Y. (1977). *Solutions of ill-posed problems.* Washington D.C.: Winston (English translation by F. John).

Wood, C. C., Cohen, D., Cuffin, B. N., & Allison, T. (1985). Electrical sources in human somatosensory cortex: Identification by combined magnetic and potential recordings. *Science, 227,* 1051–1053.

Wood, C. C., George, J. S., Lewis, P. S., Ranken, D. M., & Heller, L. (1990). Anatomical constraints for neuromagnetic source models. *Society for Neuroscience, Abstracts, 16,* 1241.

Yan, Y., Nunez, P. L., & Hart, R. T. (1991). A finite element model of the human head: Scalp potentials due to dipole sources. *Medical and Biological Engineering and Computing, 29,* 475–481.

Yuille, A. L. (1991). Deformable templates for face recognition. *Journal of Cognitive Neuroscience, 3,* 59–70.